# Article

# The Impact of Collagen Fibril Polarity on Second Harmonic Generation Microscopy

Charles-André Couture,[1] Stéphane Bancelin,[1] Jarno Van der Kolk,[2] Konstantin Popov,[2] Maxime Rivard,[1] Katherine Légaré,[1] Gabrielle Martel,[3] Hélène Richard,[3] Cameron Brown,[4] Sheila Laverty,[3] Lora Ramunno,[2] and François Légaré[1,*]
[1]Institut National de la Recherche Scientifique, Centre Énergie Matériaux Télécommunications, Varennes, Quebec, Canada; [2]Department of Physics, University of Ottawa, Ottawa, Ontario, Canada; [3]Comparative Orthopaedic Research Laboratory, Faculté de Médecine Vétérinaire, University of Montreal, Sainte Hyacinthe, Quebec, Canada; and [4]University of Oxford, Botnar Research Center, NDORMS, Oxford, United Kingdom

ABSTRACT    In this work, we report the implementation of interferometric second harmonic generation (SHG) microscopy with femtosecond pulses. As a proof of concept, we imaged the phase distribution of SHG signal from the complex collagen architecture of juvenile equine growth cartilage. The results are analyzed in respect to numerical simulations to extract the relative orientation of collagen fibrils within the tissue. Our results reveal large domains of constant phase together with regions of quasi-random phase, which are correlated to respectively high- and low-intensity regions in the standard SHG images. A comparison with polarization-resolved SHG highlights the crucial role of relative fibril polarity in determining the SHG signal intensity. Indeed, it appears that even a well-organized noncentrosymmetric structure emits low SHG signal intensity if it has no predominant local polarity. This work illustrates how the complex architecture of noncentrosymmetric scatterers at the nanoscale governs the coherent building of SHG signal within the focal volume and is a key advance toward a complete understanding of the structural origin of SHG signals from tissues.

## INTRODUCTION

Collagen is the most abundant protein in mammals and is the major component of the extracellular matrix. As such, it is involved in most of the mechanical properties of connective tissues such as their stiffness and elasticity (1–3). Nowadays, 28 different types of collagen have been identified, all being constructed from a specific assembly of polypeptide chains arranged in a triple helical structure, named tropocollagen. Among them, fibrillar collagens (mostly types I and II) self-assemble into a highly regular alignment of triple helices, with a characteristic 67 nm banding pattern (2–4). This forms the collagen fibrils that have a cylinder-like structure of a diameter of 10 to 500 nm (2–4) and a length that can reach a few tens of microns. At the macroscopic scale, the organization of collagen fibrils varies drastically from one tissue to another to comply with their physiological functions. In this article, we study the collagenous structure of cartilage that is formed at the nanoscale of a hydrated aggrecan gel reinforced by a three-dimensional collagen type II meshwork (5). At the macroscopic level, the collagen fibrils are arranged in closely linked leaves that are perpendicular to the surface deep in the cartilage and rapidly curve to become parallel to the surface in the superficial layers (6). Notably, the collagen structure in this tissue is an important indicator of the progress of

certain diseases such as osteochondrosis (7) and osteoarthritis (8,9).

Huge efforts have been made to study more precisely the structure of collagenous tissues. At first, this research used electron microscopy or mechanical imaging, such as atomic force microscopy and piezoelectric force microscopy, providing nanoscale resolution (10–14). Most of these works have imaged tissues made of type I collagen, such as tendon and fascia, mainly because of its prevalence in the human body. These techniques revealed, among other things, that the tropocollagen and the fibrils it forms are piezoelectric (15–17). Over time, optical techniques have been developed to study the structure of the collagen fibrils inside connective tissues in a minimally invasive way. Among these techniques, second harmonic generation (SHG) has proved itself to be a powerful tool to quantify the structural organization of connective tissues (18–23) because of its high specificity for dense noncentrosymmetric media such as piezoelectric structures. SHG is a nonlinear optical process in which the radiated light is at exactly half the excitation wavelength and probes the second-order nonlinear susceptibility tensor ($\chi^{(2)}$). This coherent imaging technique is characterized by an intrinsic optical sectioning, providing submicron resolution, a high penetration depth in scattering tissues and a reduced phototoxicity and photobleaching compared with other optical techniques such as fluorescence microscopy.

CrossMark

In highly anisotropic fibrillar collagen, SHG is coherently amplified because of the tight alignment of harmonophores along the collagen triple helix and within fibrils. Many studies have investigated the exact molecular and structural origin of SHG signals in biological tissues, mostly in collagen and collagenous tissues (24–27). In particular, extensive literature is available about the use of polarization-resolved second harmonic generation (P-SHG) to measure the global collagen organization (28–30). However, because of the coherence of SHG, the signal intensity depends not only on the density and the overall organization of harmonophores, but also on the relative polarity of fibrils within the focal volume. Indeed, two identical achiral noncentrosymmetric structures having opposite polarities (relative orientation of 180°) will emit $\pi$-phase-shifted SHG signal (14,31,32). Note that, if the contribution of the chiral components has been discussed at the molecular scale (33,34), the usual model for SHG in collagen fibrils assumes a $C_\infty$ symmetry (27,32,35,36), which excludes the chiral components. Because the diameter of the collagen fibrils is significantly smaller than the optical resolution, the second harmonic generated in the focal volume arises from the coherent contribution of several fibrils (32). Therefore, despite numerous studies, the analysis of SHG images remains a complex task and the structural organization of harmonophores at the submicron scale is still a matter of debate (35). SHG microscopy is indeed limited in its study of the nanoscale arrangement of the fibrils polarity because, in its usual implementation, it measures only the intensity and not the phase of the signals. This limitation can be overcome by combining SHG imaging with interferometry. Interferometric second harmonic generation (I-SHG) has been originally proposed to characterize the nonlinear properties of crystals (37–39). To the best of our knowledge, we were the first to apply this technique on biological samples and demonstrate its potential to measure the relative orientation of the SHG emitters in tissues. In previous work, focusing on tendon, we showed that the ratio of fibrils with opposite polarities globally stays close to one (11),

but varies slightly locally, revealing two predominant polarities arranged in long and thin fibril bundles (40). Another technique based on interferometric sum frequency generation (I-SFG) has recently been demonstrated to probe the collagen polarity in tendon (41).

In this work, we further investigate the structural origin of SHG signal in tissues, in particular the role of the relative polarity of SHG emitters in the coherent amplification of signal, by studying the collagen architecture within growth cartilage. However, the more random arrangement of fibrils in cartilage causes a strong decrease in SHG intensity that in turn drastically reduces the interferometric contrast within I-SHG images and impedes the investigation of the local distribution of the noncentrosymmetric structures. To overcome this limitation, we implemented I-SHG with a femtosecond laser and applied it to image biological tissues. To do so, we developed a setup that compensates for the dispersion introduced in the microscope and effectively optimizes both the spatial and temporal overlap. At first glance, I-SHG images of cartilage reveal large domains of constant SHG phase together with regions of quasi-random phase, which are correlated to respectively high- and low-intensity regions in the SHG image. We then extract information about the fibrils polarity inside each of these domains, by means of numerical simulations. Finally, comparing these results with P-SHG measurements highlights the crucial role of fibril polarity in determining the SHG signal intensity.

## MATERIALS AND METHODS

### Sample preparation

All five samples were harvested from the femoral trochleas (Fig. 1 a) of 1-day-old foals that were part of another research investigation at the Faculté de Médecine Vétérinaire, Université de Montréal. This study was carried out in strict accordance with the recommendations in the Guide for the Care and Use of Laboratory Animals of The Canadian Council on Animal Care. The protocol was approved by the Committee on the Ethics of Animal Experiments of the University of Montréal. Plugs were taken from the trochleas, fixed in 10% formalin for 24 h and decalcified in
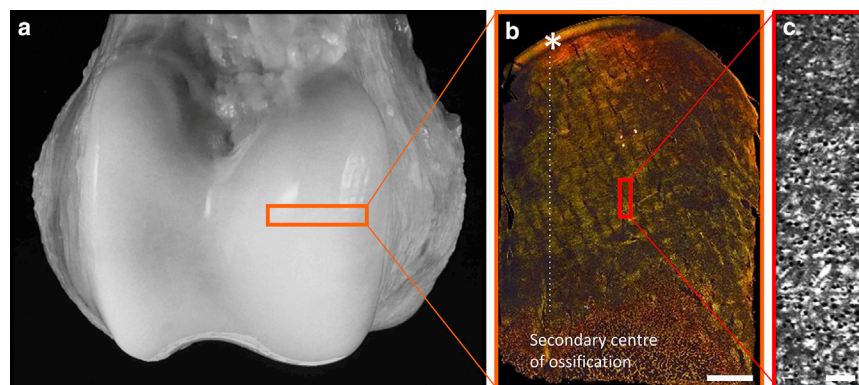


FIGURE 1  (a) Femoral trochleas from 1-day-old foals. The rectangle represents the region of interest (ROI) assessed. (b) A 4 $\mu$m thick section cut from the same region perpendicular to the articular surface, stained with picrosirius red, and imaged with polarized light microscopy to reveal the collagen structure of the articular epiphyseal growth cartilage overlying the subchondral bone in the lower part of the image. Scale bar: 2 mm. The nonvascular articular cartilage has a lamellar appearance at the surface (*white asterisk*). The vascularized epiphyseal growth cartilage of the epiphysis (*dotted line*), lies between the growth cartilage and ossification front. The rectangle represents the ROI imaged with SHG. (c) SHG image of central area of an unstained 10 $\mu$m thick cartilage slice in the central area of epiphyseal growth cartilage. Scale bar: 100 $\mu$m. To see this figure in color, go online.

EDTA for 6 to 7 days. These sections were then fixed in 70% alcohol for 1 to 2 h and embedded in paraffin. Afterward, these blocks were cut in 10 $\mu m$ thick slices with a microtome (Fig. 1 b). The obtained samples were placed on cover slips and the paraffin was removed using two xylene baths and three cycles of varying alcohol concentration baths (100%, 95%, 80%, 0%). All the images shown in this article come from the epiphyseal growth cartilage (42) of the same sample (Fig. 1 c). Importantly, although the arcade model implies that the surface collagen fibrils could bend in either direction (horizontal or out of plane here), in the imaged region, the fibrils are perpendicular to the cartilage surface (vertical here) and therefore lie in a plane or at least exhibit a very small out-of-plane angle (6,43).

## Multiphoton microscope

SHG imaging was performed using a custom-built sample scanning microscope (Fig. 2 a). Note that the asterisk (*) marked objects were not used for standard SHG microscopy but only in the I-SHG experiments described in the next section. The laser source was a Titanium-Sapphire (Ti-Sa) oscillator (Tsunami, Spectra Physics, Santa Clara, CA) generating 810 nm, 100 fs pulses at a 80 MHz repetition rate. The average power was adjusted, using a half-waveplate and a Glan-Thompson polarizer, to ~30 mW on the sample. The beam was focused through an objective (Olympus (Tokyo, Japan) Uplan-SApo, 40×, water immersion, NA 1.15) used in air, so that the effective nu-
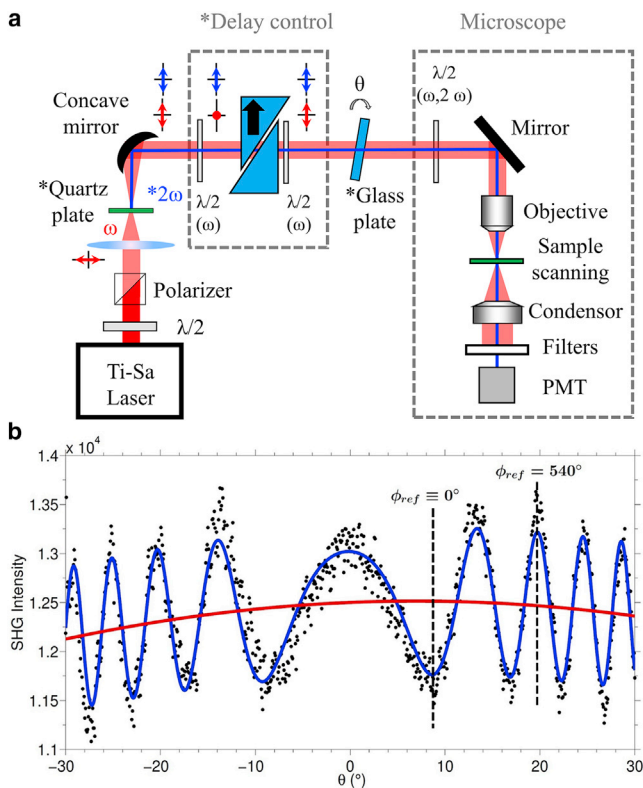


**a**

**b**

FIGURE 2 (a) Experimental setup used for SHG and I-SHG (*) microscopy. The delay control is achieved through two calcite prisms placed between two half-waveplates at 810 nm and full-waveplates at 405 nm so that the fundamental beam exhibits a retardation compared with the reference SHG beam. The black arrow indicates the optical axis. (b) Interferometric pattern obtained from the calibration of the glass plate, using a Y-cut quartz plate as the sample. This is used to link the glass plate angle to the reference phase. The blue line is the fit on the theoretical pattern described in Stolle et al. (45), modulated by a Gaussian envelope in red. To see this figure in color, go online.

merical aperture was ~0.8, to achieve typical lateral (0.6 $\mu m$) and axial (2 $\mu m$) resolutions at 810 nm excitation. Samples were placed on a translation stage (MLS203-P2, Thorlabs, Newton, NJ), and the signals were collected through a condenser with numerical aperture 0.55. Appropriate filters were used to isolate the second harmonic (two large bandpass filters FF01-720/SP-25 and a small bandpass FF01-405/10-25, Semrock, Rochester, NY), and the signals were acquired in the forward direction on a photomultiplier tube (R6357, Hamamatsu Photonics, Japan) set at 800V. We used a pixel dwell time of 25 $\mu s$; however, because of the acceleration and deceleration time of the translation stage, the acquisition time for one SHG image was typically of a few minutes. At the entrance of the microscope, a half-waveplate allowed us to adjust the incident polarization on the sample and enabled us to perform polarization-resolved second harmonic generation (P-SHG).

## Interferometric second harmonic generation setup

The I-SHG technique retrieves the phase of the SHG signal in the sample by measuring the interference of two SHG signals. The first SHG signal is generated in a quartz crystal outside the microscope, to provide a reference SHG beam with a known phase, and the second SHG signal is generated within the sample. By measuring the intensity as a function of the phase of the reference SHG ($\Phi_{ref}$), the relative phase of the SHG signal from the sample ($\Phi_{exp}$) can be retrieved pixel by pixel.

To perform I-SHG, two components need to be added to the SHG microscope setup, namely the reference quartz and the glass window, as previously described (40,44). First, the laser is loosely focused (focal length of 50 mm) on a 350 $\mu m$ thick Y-cut quartz plate, to generate the reference SHG beam. To adjust the intensity of this reference beam, the quartz plate position is moved relative to the focal point of the lens. Both fundamental and reference SHG beams are collimated by means of a curved mirror to avoid chromatic aberrations. These two beams are then carried through the microscope where the sample SHG is generated at the focus of the objective. On the detector, the two SHG beams interfere to generate the final signal, which is given, at each pixel, by the following:

$$I(\phi_{ref}) = I_{ref} + I_{exp} + 2\sqrt{I_{ref}I_{exp}}\cos(\phi_{exp} - \phi_{ref}), \quad (1)$$

where $I_{ref}$ and $I_{exp}$ are, respectively, the SHG intensity in the reference quartz and in the sample. The reference phase ($\Phi_{ref}$) is adjusted by rotating a 1.5 mm thick BK7 glass window. The exact phase relationship between the two second harmonic beams is calibrated by using a second quartz plate as the sample, obtaining an interferometric pattern (Fig. 2 b) as described by Stolle et al. (45). In the actual I-SHG images, only a small portion of this angle range is used ($\Phi_{ref} = 0°$ arbitrarily set to $\Phi_{ref} = 540°$) as only one and a half period is required for a complete characterization of the phase.

To reconstruct phase images, the interferometric term is isolated by computing the difference between two raw intensity images taken with a $\Phi_{ref}$ difference of $\pi$ in the following:

$$I(\phi_{ref}) - I(\phi_{ref} + \pi) = 4\sqrt{I_{ref}I_{exp}}\cos(\phi_{exp} - \phi_{ref}). \quad (2)$$

Finally, the acquisition of 12 pairs of images for reference phases from 0° to 330°, by increments of 30°, and a fit of the intensity as a function of $\Phi_{ref}$, using Eq. 2, allows to recover the relative phase of the sample SHG ($\Phi_{exp}$) in every pixel. As a convention, in all the following images, a red color will be assigned to the negative phase values on the I-SHG images and a green color to the positive phase values.

## Delay control

To obtain interferences, spatial and temporal overlap must be attained and both reference and sample SHG must have identical polarizations. In

previous work (40,44), we used a laser of central wavelength 1064 nm with a pulse duration of ~15 ps. This allowed us to easily achieve temporal overlap, but in consideration, drastically limited the intensity of second harmonic generated and the image contrast. In this study, to go beyond this limitation, the laser source was changed for a Titanium-Sapphire oscillator delivering femtosecond pulses. However, temporal overlap is more difficult to obtain with shorter pulses. Indeed, because of the high dispersion introduced by the microscope objective, at the focal point the reference and sample SHG exhibit a delay larger than the coherence time of the laser, which impedes the interferences.

Using a custom-built Michelson interferometer, we measured the delay between the two beams to be ~7 ps on the detector. Adjusting the length of one of the two arms in the interferometer allowed us to compensate for the dispersion and to retrieve interferences at the focus of the objective. However, because the two beams have different optical paths, this setup is very sensitive to alignment and is subject to phase fluctuations. To improve the stability of our measurements, we came back to a collinear setup, as shown in Fig. 2 a, which ensures both spatial overlap and stability, and compensates for the dispersion using two calcite wedges. A half-waveplate for the fundamental beam (full-waveplate for second harmonic) is placed before the calcite so that the fundamental and SHG beams polarizations are along orthogonal axes in the calcite (here the SHG is polarized along the optical axis). This results in a negative delay (because of abnormal dispersion) between the two beams, precompensating for the positive delay introduced in the microscope. After the calcite, the polarization of the fundamental and reference second harmonic beams are put back together using another half-waveplate at 810 nm (full-waveplate at 405 nm) so that at the entrance of

the microscope the reference SHG has the same polarization as the fundamental beam.

## RESULTS

### I-SHG of growth cartilage

Fig. 3 a shows the SHG image of the studied cartilage sample. In this image, the black circles correspond to chondrocyte lacunae, or spaces in the matrix where the chondrocytes resided. Here two types of regions can be distinguished. First, a large part of the image has a speckle-like aspect, with low average SHG intensity. This is expected from the general cartilage structure that is comprised of a random-like collagen type II meshwork (10). However, several regions, mostly around the cells, exhibit a high and almost uniform SHG signal. Fig. 3 b shows the I-SHG image of the sample at the exact same position and indicates the SHG relative phase measured pixel by pixel. Pixels with low SHG intensity (below 50 counts), such as the pixels within the cells, are displayed in yellow. They are rejected from analysis, as their phase is not well defined, and they do not carry any structural information. We directly observe that the I-SHG image presents large domains in which the
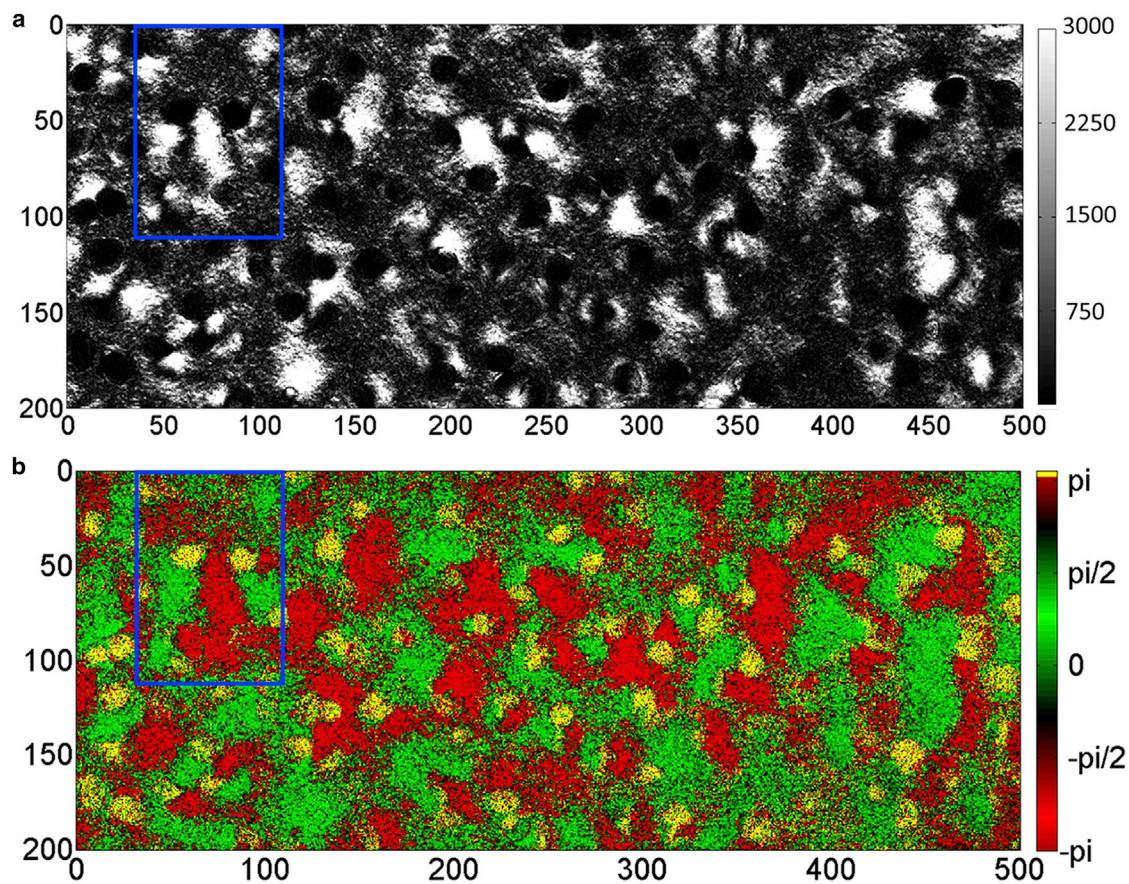


FIGURE 3   (a) SHG image and (b) I-SHG image of cartilage (images are graduated in microns). The blue rectangle indicates the ROI used in Fig. 4. Pixels with SHG intensity below 50 counts are displayed in yellow in the I-SHG image. To see this figure in color, go online.

phase is constant over distances of the order of 20 to 50 $\mu m$. Interestingly, these domains seem to be colocalized with the high-intensity regions in the standard SHG image.

To investigate the relationship between the intensity and the phase image, we analyzed in details a smaller region of interest (ROI), depicted by the blue rectangle in Fig. 3, $a$ and $b$, where we can observe different behaviors, in particular a phase transition. Fig. 4, $a$ and $b$, show, respectively, the SHG intensity and phase for this ROI.

In Fig. 4, $a$ and $b$, two subregions are identified: the bottom rectangles indicate a region of high intensity and well-defined phase, with two opposite main phase values (*red and green*) and a transition zone (*blue*), whereas the top rectangle shows a region of low intensity and random phase (speckle-like aspect). The distribution of phase in these regions can be studied by looking at the phase histograms, shown in Fig. 4, $c$–$f$. This shows that the regions highlighted in green (Fig. 4 $d$) and red (Fig. 4 $f$) have a well-defined phase assembled in a sharp peaked distribution. As expected from the phase image, these peaks are approximately $\pi$-phase-shifted, denoting opposite fibrils' polarity. In contrast, the phase distributions of the speckle (Fig. 4 $c$) and the transition (Fig. 4 $e$) regions are composed of two large peaks, which indicates that both fibril polarities are present in those regions. Importantly, the green and red regions exhibit high SHG intensity whereas the blue and yellow regions show lower signals.

## Polarization analysis

To characterize more precisely the different regions identified in the cartilage, we used P-SHG to investigate the role of collagen fibrils anisotropy in these areas. Here again, four zones are analyzed (Fig. 5 $a$): pixels from the green and red phase peaks in Fig. 4 $b$, the transition zone between these two peaks (in *blue*), and the speckle-like region (in *yellow*). For each region, we measured the intensity pixel by pixel, as a function of the input polarization. One such polar plot is shown in Fig. 5 $b$ and shows the behavior of the pixels in the red square. On this polar plot, we measure the maximum intensity $I_{par}$, which is obtained when the incident polarization angle ($\psi$) is parallel to the fibrils' main axis, and the intensity $I_{perp}$, which corresponds to an incident polarization perpendicular to the fibrils, and therefore a minimum intensity. Finally, we characterize the anisotropy of the polarization response using the parameter ($r$), calculated pixel by pixel in the following:

$$r = \frac{I_{par} - I_{perp}}{I_{par} + 2I_{perp}}. \qquad (3)$$

This measurement is inspired by the anisotropy parameter from Campagnola et al. (46) and serves as a measure of the structural organization of the collagen fibrils in the studied regions.

Fig. 5, $c$ and $d$, show, respectively, the mean anisotropy and the mean SHG intensity over the pixels for the different ROIs. Statistical analysis has been performed using Origin 9.0 (OriginPro 9.0 SR2, OriginLab, Northampton, MA). As the normality of the distribution has been rejected using Shapiro-Wilk's test, the difference of the distributions has been determined using the Wilcoxon-Mann-Whitney test. Fig. 5 $c$ reveals similar anisotropy between the pixels in the green and the red peaks, indicating the same degree of
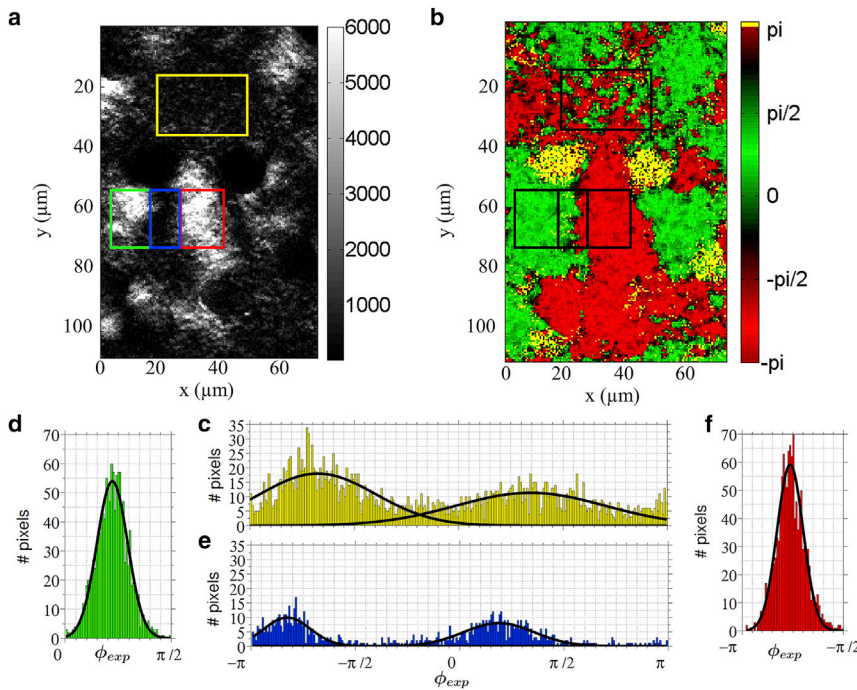


FIGURE 4 (*a*) SHG image and (*b*) I-SHG image of cartilage (*blue rectangle* of Fig. 3). Pixels with SHG intensity lower than 50 counts are displayed in yellow. (*c*–*f*) The histograms of $\Phi_{exp}$ in the rectangles in (*a*) and (*b*). The lines over the data are Gaussian fits. The histogram (*c*) (calculated over 2400 pixels) has two phase peaks at $-0.67\pi$ with $\sigma = \pi/4 \pm \pi/50$ and at $0.34\pi$ with $\sigma = \pi/3 \pm \pi/50$. The green histogram in (*d*) (calculated over 1500 pixels) has only one peak at $0.22\pi$ with $\sigma = \pi/14 \pm \pi/600$. The blue histogram in (*e*) (calculated over 500 pixels) has two peaks at $-0.83\pi$ with $\sigma = \pi/9 \pm \pi/150$ and at $0.24\pi$ with $\sigma = \pi/6 \pm \pi/120$. The red histogram in (*f*) (calculated over 1500 pixels) has only one peak at $-0.76\pi$ with $\sigma = \pi/16 \pm \pi/1000$. To see this figure in color, go online.
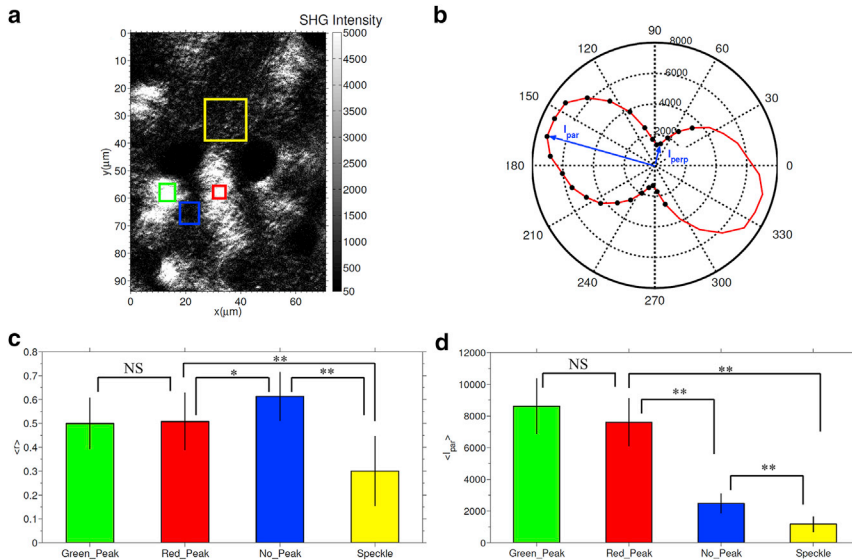
FIGURE 5 (*a*) SHG image of cartilage. (*b*) Polar plot of the SHG intensity as a function of the incident polarization. The black circles correspond to the experimental measurements obtained from $\psi = 45°$ to $\psi = 285°$, and the red line shows the extension of these measurements on a full 0° to 360° range. The blue arrows indicate the maximum ($I_{par}$) and minimum ($I_{perp}$) intensity used to compute the anisotropy parameter $r$. (*c* and *d*) Bar plots of respectively the mean anisotropy and the mean SHG intensity for polarization parallel to the collagen fibrils over the pixels in the corresponding rectangles in (*a*). The error bars indicate the standard deviations calculated over all the pixels (respectively 420, 256, 648, and 2601 pixels) in the ROIs. Statistical significance was tested using nonparametric Wilcoxon-Mann-Whitney (NS, no significant difference, *$p < 0.05$, **$p < 0.01$). To see this figure in color, go online.

alignment in the two bright regions. The blue ROI has a slightly larger anisotropy, which denotes a higher degree of alignment. The yellow region presents a lower anisotropy, i.e., more randomly aligned fibrils. Fig. 5 *d* shows that, as expected, the pixels in the yellow region (speckle-like aspect) present also a low average SHG signal whereas the red and green pixels have similarly high maximum intensity levels. However, the blue region, located between the two peaks, presents surprisingly a high anisotropy and a low value of $<I_{par}>$. Note that in the blue ROI, even if the value of $<I_{par}>$ is lower than in the green and red ROI, the signal reaches 2000 counts that is ~40 times higher than the noise (50 counts) in our image.

## Numerical simulations

To further investigate the link between the SHG intensity and the phase distributions we implemented numerical simulations. For a complete description of the model used, see Rivard et al. (40). Briefly, collagen fibrils are modeled as a series of parallel cylinders that all have a $\chi^{(2)}$ with the same amplitude and a sign that can vary inside the tissue, representing the two polarities of the fibrils. The SHG contribution from each cylinder is then calculated in the far-field using a Green's function approach and summed up to calculate the signal on the detector. Here, a beam of waist 1.1 $\mu m$ and of wavelength 810 nm is sent on the tissue that is considered having a uniform refractive index of 1.4.

Individually, two fibrils with opposite polarities generate $\pi$-phase-shifted signal. As SHG results from the coherent summation of several fibrillar responses in every pixel, the relative polarity between adjacent fibrils can highly affect the signal intensity. Therefore, the tissue is defined by the following parameter $f$ that indicates the number of fibrils with positive polarity:

$$f = \frac{N(+\chi^{(2)})}{N(+\chi^{(2)}) + N(-\chi^{(2)})}, \tag{4}$$

where $N(\pm\chi^{(2)})$ indicates the number of fibrils in the tissue with $\pm\chi^{(2)}$. For tissues with different $f$ ratios (1000 random generated samples for each $f$ value), the SHG signal is computed and its phase distribution extracted.

The Fig. 6 *a* presents the $f$ ratio as a function of the standard deviation of the phase distribution (*black circles*) along with a spline fitting (*black line*). This allows to extract the $f$ ratios from the standard deviations of the phase distributions found for each region of the cartilage analyzed here. The colored squares indicate the experimental measurements in the different ROIs. It is worth noting that in the simulations, the absolute phase of each fibril is known, allowing to retrieve the exact phase histogram with its standard deviation. However, when the inverse relation is investigated, two possible $f$ ratios can be found for each value of standard deviation, with no possible way of distinguishing between the two cases. Again, by convention, we associate negative phase (*red pixels*) to $f$ ratios larger than 0.5.

In the ROIs identified earlier, we calculated, using the spline fit on Fig. 6 *a*, that the relative number of fibrils with positive polarity is given by $f = 0.30$ in the green rectangle and $f = 0.72$ for the red rectangle. The blue and yellow regions present phase distributions with two peaks, indicating a $f$ ratio varying on average between $f = 0.39$ and $f = 0.65$ (*blue rectangle*) and between $f = 0.44$ and $f = 0.59$ (*yellow rectangle*). Here, the measured parameter was the standard deviation of the phase distributions ($\sigma$) from which we extracted the ratio of fibrils with $+\chi^{(2)}$ over the total number of fibrils ($f$ ratio). It is worth noting that the numerical model used here only describes correctly
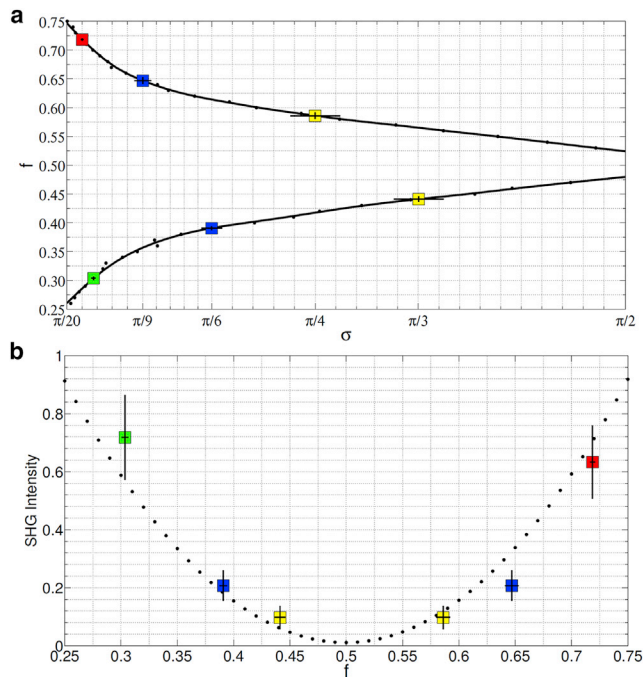
FIGURE 6 (a) f ratio as a function of the standard deviation of the phase distribution. The black dots are obtained by numerical simulations, the black line is a spline, and the colored rectangles represent the calculated f ratios corresponding to the same-colored regions in Fig. 4. (b) Normalized value of the mean SHG intensity in function of the f ratio. The black dots are the results from the numerical simulations (average over 1000 random samples) and the colored rectangles are the experimental <I_{par}>, corresponding, respectively, to the same-colored rectangles in Fig. 4. Error bars indicate the standard deviations. Here the x-value of (a) (σ) and the y-value of (b) (SHG intensity) are measured parameters whereas the f ratio is calculated numerically. The similarity between experimental and calculated data was evaluated with Pearson's chi-squared test ($p < 2.2\ 10^{-16}$) using R software (R Development Core Team, R Foundation for Statistical Computing, version 3.0.3). To see this figure in color, go online.

regions of high anisotropy and therefore the f ratio extracted in the speckle-like region (*yellow ROI*) is not quantitative but only indicative. Fig. 6 b displays the mean SHG intensity as a function of the f ratio. The black dots have been calculated numerically using the same simulations as in Fig. 6 a. We also report the maximum intensities $I_{par}$ found experimentally as a function of the extracted f ratio for the corresponding regions (*colored squares*).

## DISCUSSION

Our numerical simulations show that in a tissue with a global f ratio equal to 0.5, i.e., a random distribution of polarity, the phase constantly varies from pixel to pixel that results in a very broad distribution on the histogram. On the contrary, a f ratio of 0.0 or 1.0 indicates that only one polarity is present in the tissue and that all pixels will have the same phase. Therefore, the more the f ratio is away from 0.5, the more the phase is locked to a fixed value and the

more the histogram is peaked around this value. Interestingly, the very good correlation between the numerical and experimental points in Fig. 6 b illustrates the strength of I-SHG in understanding the origin of the signal and indicates that the variations of the f ratio in the field of view is indeed responsible for the intensity variations observed in the standard SHG images.

We can now fully interpret the different behaviors observed in Fig. 5, c and d. First, it appears that the pixels in the yellow region present simultaneously a low anisotropy, a f ratio close to 0.5, and a low average SHG intensity. This has been previously discussed in the literature (47) and results from the coherent summation of the SHG signals arising from several collagen fibrils with various azimuthal angles and polarities in the focal volume. On the contrary, the red and green ROIs in the bottom of Fig. 4 b present a high anisotropy and a f ratio quite far from 0.5 that results in a high SHG intensity because of almost fully constructive interferences. Finally, in the transition zone indicated by the blue ROI, the anisotropy is still high, the f ratio gets closer to 0.5, and the intensity is very low. Indeed, the f ratio close to 0.5 reveals an absence of predominant polarity, which results in a more random phase from one pixel to another, causing a strong drop of SHG intensity. Hence, it appears that even a well-aligned region, as revealed by P-SHG, can generate low SHG intensity if it has a f ratio close to 0.5, and therefore no predominant polarity. It is worth noting that, in both sides of the low intensity blue area in Fig. 4 b, despite a predominant polarity, revealed by the constant red and green color, the f ratio is closer to 0.5 than in the red and green regions. Therefore, a constant color in I-SHG is not enough to obtain a high SHG intensity and it is really the f ratio, or equivalently the phase distribution, that governs the level of signal.

To summarize, by looking at the phase only we can distinguish three cases.

1) There is a predominant polarity in the domain (red or green color) and the f ratio is far from 0.5. This is the case of the red and green rectangles in Fig. 4 a, which corresponds to high SHG intensity.
2) There is a predominant polarity (constant color) but the f ratio is close to 0.5. In this case, $f-0.5$ is close to 0 but has a constant sign. This is what happens in both sides of the blue rectangle that corresponds to a quite low SHG intensity.
3) There is no predominant polarity (random color in the phase image). In this case, $f-0.5$ is always close to 0 and its sign changes randomly from one pixel to another. This is what happens in the speckle-like region that corresponds to a dark region in the SHG image.

Importantly, these observations can be generalized to the whole field of view as shown in Fig. 7 a that merges Fig. 3, a and b, by displaying the SHG intensity and phase as the value and the hue of the color, respectively. It appears that
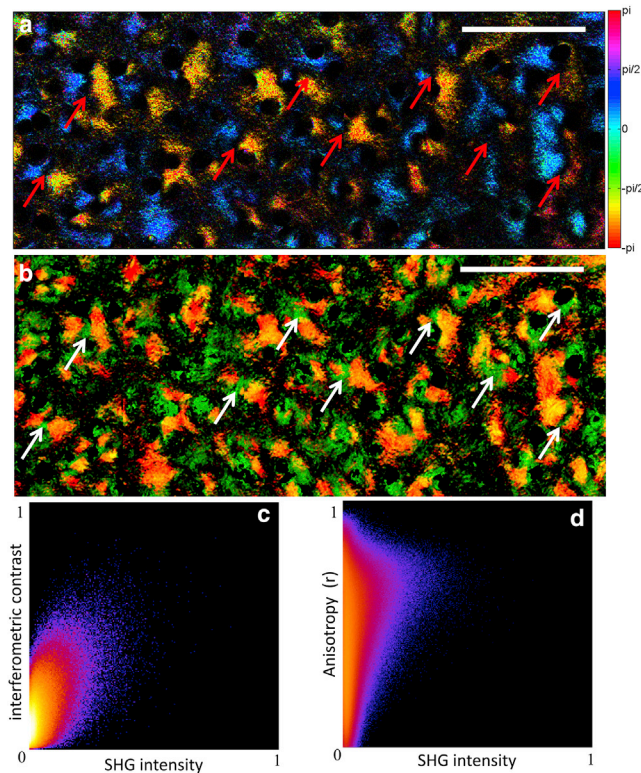
FIGURE 7  (a) HSV image merging Fig. 3, a and b, in which the SHG intensity and phase are represented respectively by the value and the hue of the color. Red arrows indicate regions similar to the blue ROI in Fig. 4 a with a phase transition corresponding to a low SHG intensity. Scale bar: 100 $\mu$m. (b) Image merging the SHG intensity (red) and the map of anisotropy parameter r (green). White arrows highlight regions of high anisotropy but low SHG intensity (no red). Scale bar: 100 $\mu$m. (c) Correlation histogram between the SHG intensity and the interferometric contrast (Pearson coefficient 0.6). (d) Correlation histogram between the SHG intensity and the anisotropy parameter (Pearson coefficient 0.3). To see this figure in color, go online.

the bright regions correspond to constant phase domains whereas the transitions between two phase domains are always low SHG intensity areas as highlighted by the red arrows.

Fig. 7 b shows the merging of the SHG intensity (in red) and the anisotropy parameter (in green) in the same field of view. Similarly to the yellow ROI in Fig. 5 a, we observe large regions of low anisotropy and low intensity. However, we observe several regions of high anisotropy and low SHG intensity as indicated by the white arrows. This is consistent with the results observed in the smaller area (see blue ROI in Fig. 5) and reveals that at the scale of the field of view, the anisotropy parameter is not the only responsible for the variations of intensity in the SHG image of cartilage.

To further investigate the similarities between phase, anisotropy, and intensity images, on a pixel-by-pixel basis, we used correlation analysis and determined the Pearson coefficient over the entire field of view. When the two images are perfectly similar, the Pearson coefficient is 1.0 and falls

to 0.0 when no correlation exists. We obtain a Pearson coefficient of 0.6 for the correlation between interferometric contrast and intensity image and 0.3 for the correlation between the anisotropy and the intensity. It is worth noting that a perfect correlation is not expected as both the anisotropy and the phase independently affect the intensity. Fig. 7, c and d, allows us to visualize this correlation graphically, displaying the overlap of the intensity distribution (x axis) with the interferometric contrast and anisotropy parameter distribution (y axis), respectively, where, for a perfect correlation all points would fall on the diagonal. These values and graphs indicate a stronger correlation between the phase and the intensity compared with the anisotropy and the intensity that confirms the qualitative observation on Fig. 7, a and b. This highlights the crucial role of the phase in determining the SHG intensity and indicates that the polarity of collagen fibrils should not be neglected when interpreting SHG images of collagenous tissues.

The two images in Fig. 7, a and b, carry a lot of information about the structure of collagen in articular cartilage. The dark areas, common in both images, indicate that the collagen fibrils are organized in a loose, quasi-isotropic meshwork, both in terms of orientation and polarity. On the contrary, we observe areas of high anisotropy parameter and low SHG intensity, which reveals a well-aligned collagen meshwork but with an almost random polarity. Finally, the regions of high anisotropy and high intensity correspond to areas where the collagen fibrils are well aligned with a constant polarity.

These regions of highly aligned collagen fibrils with similarly polarized domains are almost exclusively located in the neighborhood region of the chondrocytes, leading us to speculate on the potential biological roles of the observed structures. The highly specialized architecture of collagen in the chondron and territorial matrix has been studied extensively, particularly to relate its structure to function (48). Notably, it has been shown (43,49) that this region in articular cartilage has a preferential orientation and a more aligned collagen matrix than the bulk of the extracellular matrix. This is reflected in P-SHG images showing regions of high anisotropy around the cells, which confirm that the collagen fibrils are more aligned in the neighborhood of chondrocytes than the fibrils in the disordered meshwork of the interterritorial matrix. The dominant polarity of these regions switches across the cells, typically in the radial (bone-to-surface) direction. The consistency of this switching suggests a potential for local cell signaling. As collagen is piezoelectric in shear ($d_{15} \approx 1$ pm/V) (14,50), this switching of domain will produce a similar polarity of electrical potential on both sides of the cell under shear. The predominant direction of the polarity switch thus conforms to the predominant direction of shear stresses in cartilage (in a plane perpendicular to the surface), which are on the order of 2 MPa (51,52).

In addition to the strong alignment, I-SHG indicates that there is a high level of domain switching within the

observed regions of dominant polarity. This may facilitate fibril slipping, and play a role in the different mechanical properties of the territorial compared with the interterritorial matrix, in particular the lower elastic modulus observed around the chondrocytes (53). It may further assist the formation of the radial bundles observed around cells during development (48). The preferential polarity of fibrils observed in these healthy samples, however, may provide seed points for later degenerative changes. Here, larger-scale local bundling of fibrils drives a loss of cohesive strength of the matrix (54) and is a physical hallmark of disease (55). In previous (noninterferometric) SHG studies of early-stage osteoarthritic cartilage, we observed an increase in fibril bundling with disease (9), and through mechano-structural modeling have identified such bundles as a mechanically irreversible step in the disease process (8).

## CONCLUSIONS

In this article, SHG and I-SHG microscopy have been used to image the structure and polarity of collagen type II fibrils in juvenile equine growth cartilage. The organization of collagen fibrils, measured with P-SHG, exhibits two behaviors: regions of random organization and domains of high fibrillar alignment. As expected, the regions of random organization generate low and speckle-like SHG intensity. I-SHG reveals that these regions also have a random phase. However, it appears that a domain of high fibrillar alignment does not necessarily result in a strong SHG intensity, depending on its phase distribution. Extracting the $f$ ratio, which quantifies how predominant a polarity is in a studied region, we explain the low SHG intensity in the aforementioned region of high anisotropy as the result of a $f$ ratio close to 0.5. Indeed, a quasi-random distribution of the fibril polarity inside the focal volume leads to destructive interferences and therefore to a sharp decrease in SHG intensity. Hence, I-SHG provides the first experimental evidence, to our knowledge, that a preferential orientation, or equivalently a phase relationship between neighboring emitters, is required to generate a high SHG intensity, even if the fibrils are well organized.

The distribution of polarity observed in articular cartilage reveals a high correlation between the cells and the phase domains. In particular, the presence of two phase domains around the cells indicates a role of the fibril polarity in cell signaling. Finally, the flipping of the polarity in the highly aligned region around the chondrocytes may be related to the decrease in elastic modulus in the territorial matrix that suggest an important role of the fibrils polarity in determining the mechanical properties of cartilage. Finally, I-SHG appears as a powerful fixation-free technique to optically investigate the relative polarity of collagen fibrils in a wide range of tissues and will provide key insights into collagen's piezoelectric properties, which has been shown to influence the structural and mechanical properties of connective tissues as well as their growth, repair, and signaling mechanisms (56–58).

## AUTHOR CONTRIBUTIONS

## REFERENCES

1. Prockop, D. J., and K. I. Kivirikko. 1995. Collagens: molecular biology, diseases, and potentials for therapy. *Annu. Rev. Biochem.* 64:403–434.

2. Hulmes, D. J. S. 2002. Building collagen molecules, fibrils, and suprafibrillar structures. *J. Struct. Biol.* 137:2–10.

3. Kadler, K. E., C. Baldock, …, R. P. Boot-Handford. 2007. Collagens at a glance. *J. Cell Sci.* 120:1955–1958.

4. Kadler, K. E., D. F. Holmes, …, J. A. Chapman. 1996. Collagen fibril formation. *Biochem. J.* 316:1–11.

5. Berkenblit, S. I., T. M. Quinn, and A. J. Grodzinsky. 1995. Molecular electromechanics of cartilaginous tissues and polyelectrolyte gels. *J. Electrost.* 34:307–330.

6. Jeffery, A. K., G. W. Blunn, …, G. Bentley. 1991. Three-dimensional collagen architecture in bovine articular cartilage. *J. Bone Joint Surg. Br.* 73:795–801.

7. Laverty, S., and C. Girard. 2013. Pathogenesis of epiphyseal osteochondrosis. *Vet. J.* 197:3–12.

8. Brown, C. P., M.-A. Houle, …, H. S. Gill. 2012. Damage initiation and progression in the cartilage surface probed by nonlinear optical microscopy. *J. Mech. Behav. Biomed. Mater.* 5:62–70.

9. Brown, C. P., M.-A. Houle, …, F. Légaré. 2014. Imaging and modeling collagen architecture from the nano to micro scale. *Biomed. Opt. Exp.* 5:233–243.

10. Page, S. G., and H. E. Huxley. 1963. Filament lengths in striated muscle. *J. Cell Biol.* 19:369–390.

11. Parry, D. A. D., and A. S. Craig. 1977. Quantitative electron microscope observations of the collagen fibrils in rat-tail tendon. *Biopolymers.* 16:1015–1031.

12. Xia, Y., and K. Elder. 2001. Quantification of the graphical details of collagen fibrils in transmission electron micrographs. *J. Microsc.* 204:3–16.

13. Denning, D., S. Alilat, …, B. J. Rodriguez. 2012. Visualizing molecular polar order in tissues via electromechanical coupling. *J. Struct. Biol.* 180:409–419.

14. Harnagea, C., M. Vallières, …, A. Gruverman. 2010. Two-dimensional nanoscale structural and functional imaging in individual collagen type I fibrils. *Biophys. J.* 98:3070–3077.

15. Fukada, E., and I. Yasuda. 1964. Piezoelectric effects in collagen. *Jap. J. App. Phys.* 3:117.

16. Athenstaedt, H. 1974. Pyroelectric and piezoelectric properties of vertebrates. *Ann. N. Y. Acad. Sci.* 238:68–94.

17. Chepel', V. F., and V. V. Lavrent'ev. 1978. Piezoelectric effect in collagen structures. *Polymer Mech.* 14:574–579.

18. Yeh, A. T., M. J. Hammer-Wilson, …, G. M. Peavy. 2005. Nonlinear optical microscopy of articular cartilage. *Osteoarthritis Cartilage.* 13:345–352.

19. Bancelin, S., A. Nazac, …, A. De Martino. 2014. Determination of collagen fiber orientation in histological slides using Mueller microscopy and validation by second harmonic generation imaging. *Opt. Express.* 22:22561–22574.

20. Pfeffer, C. P., B. R. Olsen, …, F. Légaré. 2008. Multimodal nonlinear optical imaging of collagen arrays. *J. Struct. Biol.* 164:140–145.

21. Rivard, M., M. Laliberté, …, F. Légaré. 2010. The structural origin of second harmonic generation in fascia. *Biomed. Opt. Express.* 2:26–36.

22. Latour, G., I. Gusachenko, …, M.-C. Schanne-Klein. 2012. In vivo structural imaging of the cornea by polarization-resolved second harmonic microscopy. *Biomed. Opt. Express.* 3:1–15.

23. Miri, A. K., U. Tripathy, …, P. W. Wiseman. 2012. Nonlinear laser scanning microscopy of human vocal folds. *Laryngoscope.* 122:356–363.

24. Mertz, J., and L. Moreaux. 2001. Second-harmonic generation by focused excitation of inhomogeneously distributed scatterers. *Opt. Commun.* 196:325–330.

25. Légaré, F., C. Pfeffer, and B. R. Olsen. 2007. The role of backscattering in SHG tissue imaging. *Biophys. J.* 93:1312–1320.

26. Bancelin, S., C. Aimé, …, M.-C. Schanne-Klein. 2014. Determination of collagen fibril size via absolute measurements of second-harmonic generation signals. *Nat. Commun.* 5:4920.

27. Rocha-Mendoza, I., D. R. Yankelevich, …, A. Knoesen. 2007. Sum frequency vibrational spectroscopy: the molecular origins of the optical second-order nonlinearity of collagen. *Biophys. J.* 93:4433–4444.

28. Stoller, P., K. M. Reiser, …, A. M. Rubenchik. 2002. Polarization-modulated second harmonic generation in collagen. *Biophys. J.* 82:3330–3342.

29. Yasui, T., Y. Tohno, and T. Araki. 2004. Determination of collagen fiber orientation in human tissue by use of polarization measurement of molecular second-harmonic-generation light. *Appl. Opt.* 43:2861–2867.

30. Mansfield, J. C., C. P. Winlove, …, S. J. Matcher. 2008. Collagen fiber arrangement in normal and diseased cartilage studied by polarization sensitive nonlinear microscopy. *J. Biomed. Opt.* 13:044020.

31. Boyd, R. W. 2008. Nonlinear Optics, 3rd ed. Academic Press, San Diego, CA.

32. Stoller, P., P. M. Celliers, …, A. M. Rubenchik. 2003. Quantitative second-harmonic generation microscopy in collagen. *Appl. Opt.* 42:5209–5219.

33. Reiser, K. M., A. B. McCourt, …, A. Knoesen. 2012. Structural origins of chiral second-order optical nonlinearity in collagen: amide I band. *Biophys. J.* 103:2177–2186.

34. Perry, J. M., A. J. Moad, …, G. J. Simpson. 2005. Electronic and vibrational second-order nonlinear optical properties of protein secondary structural motifs. *J. Phys. Chem. B.* 109:20009–20026.

35. Tuer, A. E., S. Krouglov, …, V. Barzda. 2011. Nonlinear optical properties of type I collagen fibers studied by polarization dependent second harmonic generation microscopy. *J. Phys. Chem. B.* 115:12759–12769.

36. Deniset-Besseau, A., J. Duboisset, …, M.-C. Schanne-Klein. 2009. Measurement of the second-order hyperpolarizability of the collagen triple helix and determination of its physical origin. *J. Phys. Chem. B.* 113:13437–13445.

37. Rechsteiner, P., J. Hulliger, and M. Flörsheimer. 2000. Phase-sensitive second harmonic microscopy reveals bipolar twinning of Markov-type molecular crystals. *Chem. Mater.* 12:3296–3300.

38. Yazdanfar, S., L. Laiho, and P. So. 2004. Interferometric second harmonic generation microscopy. *Opt. Express.* 12:2739–2745.

39. Kaneshiro, J., Y. Uesu, and T. Fukui. 2010. Visibility of inverted domain structures using the second harmonic generation microscope: comparison of interference and non-interference cases. *J. Opt. Soc. Am. B.* 27:888–894.

40. Rivard, M., K. Popov, …, F. Légaré. 2014. Imaging the noncentrosymmetric structural organization of tendon with Interferometric Second Harmonic Generation microscopy. *J. Biophotonics.* 7:638–646.

41. Han, Y., V. Raghunathan, …, N. H. Ge. 2013. Mapping molecular orientation with phase sensitive vibrationally resonant sum-frequency generation microscopy. *J. Phys. Chem. B.* 117:6149–6156.

42. Cluzel, C., L. Blond, …, S. Laverty. 2013. Foetal and postnatal equine articular cartilage development: magnetic resonance imaging and polarised light microscopy. *Eur. Cell. Mater.* 26:33–48.

43. Hughes, L. C., C. W. Archer, and I. ap Gwynn. 2005. The ultrastructure of mouse articular cartilage: collagen orientation and implications for tissue functionality. A polarised light and scanning electron microscope study and review. *Eur. Cell. Mater.* 9:68–84.

44. Rivard, M., C.-A. Couture, …, F. Légaré. 2013. Imaging the bipolarity of myosin filaments with Interferometric Second Harmonic Generation microscopy. *Biomed. Opt. Express.* 4:2078–2086.

45. Stolle, R., G. Marowsky, …, G. Berkovic. 1996. Phase measurements in nonlinear optics. *Appl. Phys. B.* 63:491–498.

46. Campagnola, P. J., and L. M. Loew. 2003. Second-harmonic imaging microscopy for visualizing biomolecular arrays in cells, tissues and organisms. *Nat. Biotechnol.* 21:1356–1360.

47. Gusachenko, I., V. Tran, …, M.-C. Schanne-Klein. 2012. Polarization-resolved second-harmonic generation in tendon upon mechanical stretching. *Biophys. J.* 102:2220–2229.

48. Poole, C. A. 1997. Articular cartilage chondrons: form, function and failure. *J. Anat.* 191:1–13.

49. Hunziker, E. B., E. Kapfinger, and J. Geiss. 2007. The structural architecture of adult mammalian articular cartilage evolves by a synchronized process of tissue resorption and neoformation during postnatal development. *Osteoarthritis Cartilage.* 15:403–413.

50. Kalinin, S. V., B. J. Rodriguez, …, A. Gruverman. Electromechanical imaging of biological systems with sub-10 nm resolution. arXiv:cond-mat/0504232v1.

51. Henak, C. R., G. A. Ateshian, and J. A. Weiss. 2014. Finite element prediction of transchondral stress and strain in the human hip. *J. Biomech. Eng.* 136:021021.

52. Thambyah, A., and N. Broom. 2006. Micro-anatomical response of cartilage-on-bone to compression: mechanisms of deformation within and beyond the directly loaded matrix. *J. Anat.* 209:611–622.

53. Wilusz, R. E., J. Sanchez-Adams, and F. Guilak. 2014. The structure and function of the pericellular matrix of articular cartilage. *Matrix Biol.* 39:25–32.

54. Broom, N., M.-H. Chen, and A. Hardy. 2001. A degeneration-based hypothesis for interpreting fibrillar changes in the osteoarthritic cartilage matrix. *J. Anat.* 199:683–698.

55. Broom, N. D., and R. Flachsmann. 2003. Physical indicators of cartilage health: the relevance of compliance, thickness, swelling and fibrillar texture. *J. Anat.* 202:481–494.

56. Bassett, C. A. L., and R. J. Pawluk. 1972. Electrical behavior of cartilage during loading. *Science.* 178:982–983.

57. Lotke, P. A., J. Black, and S. Richardson. 1974. Electromechanical properties in human articular cartilage. *J. Bone Joint Surg. Am.* 56:1040–1046.

58. Minary-Jolandan, M., and M.-F. Yu. 2009. Nanoscale characterization of isolated individual type I collagen fibrils: polarization and piezoelectricity. *Nanotechnology.* 20:085706.